















An AGN with an ionized gas outflow in a massive quiescent galaxy in a protocluster at $z = 3.09$

MARIKO KUBO ¹, HIDEKI UMEHATA ^{2,3}, YUICHI MATSUDA ^{4,5}, MASARU KAJISAWA ¹, CHARLES C. STEIDEL ⁶,
TORU YAMADA,⁷ ICHI TANAKA ⁸, BUNYO HATSUKADE ⁹, YOICHI TAMURA ¹⁰, KOUICHIRO NAKANISHI ^{4,5},
KOTARO KOHNO ^{9,11}, KIANHONG LEE ⁹, KEIICHI MATSUDA,¹⁰ YIPING AO ^{12,13}, TOHRU NAGAO ¹
AND MIN S. YUN ¹⁴

¹*Ehime University, 2-5 Bunkyo-cho, Matsuyama, Ehime 790-8577, Japan*

²*Institute of Advanced Research, Graduate School of Science, Nagoya University, Furo-cho, Chikusa-ku, Nagoya, Aichi 464-8601, Japan*

³*Institute for Cosmic Ray Research, The University of Tokyo, 5-1-5 Kashiwa-no-Ha, Kashiwa City, Chiba, 277-8582, Japan*

⁴*National Astronomical Observatory of Japan, 2-21-1 Osawa, Mitaka, Tokyo 181-8588, Japan*

⁵*Department of Astronomy, Graduate School of Science, The University for Advanced Studies, SOKENDAI, Mitaka, Tokyo 181-8588, Japan*

⁶*Cahill Center for Astronomy and Astrophysics, California Institute of Technology, MC 249-17, Pasadena, CA 91125, USA*

⁷*Institute of Space and Aeronautical Science, Japanese Aerospace Exploration Agency, 3-1-1, Yoshinodai, Chuo-ku, Sagami-hara, Kanagawa, 252-5210, Japan*

⁸*Subaru Telescope, National Astronomical Observatory of Japan, 650 North A'ohoku Place, Hilo, HI 96720, U.S.A.*

⁹*Institute of Astronomy, Graduate School of Science, The University of Tokyo, 2-21-1 Osawa, Mitaka, Tokyo 181-0015, Japan*

¹⁰*Department of Physics, Nagoya University, Furo-cho, Chikusa-ku, Nagoya, Aichi 464-8601, Japan*

¹¹*Research Center for the Early Universe, The University of Tokyo, 7-3-1 Hongo, Bunkyo-ku, Tokyo 113-0033, Japan*

¹²*Purple Mountain Observatory and Key Laboratory for Radio Astronomy, Chinese Academy of Sciences, Nanjing, China*

¹³*School of Astronomy and Space Science, University of Science and Technology of China, Hefei, China*

¹⁴*Department of Astronomy, University of Massachusetts, Amherst, MA 01003, USA*

(Received XX XX, 20XX; Revised XX XX, 20XX; Accepted XX XX, 20XX)

Submitted to ApJ

ABSTRACT

We report the detection of an ionized gas outflow from an X -ray active galactic nucleus (AGN) hosted in a massive quiescent galaxy in a protocluster at $z = 3.09$ (J221737.29+001823.4). It is a type-2 QSO with broad ($W_{80} > 1000 \text{ km s}^{-1}$) and strong ($\log(L_{[\text{O III}]}) / \text{erg s}^{-1} \approx 43.4$) $[\text{O III}]\lambda\lambda 4959, 5007$ emission lines detected by slit spectroscopy in three-position angles using Multi-Object Infra-Red Camera and Spectrograph (MOIRCS) on the Subaru telescope and the Multi-Object Spectrometer For Infra-Red Exploration (MOSFIRE) on the Keck-I telescope. In the all slit directions, $[\text{O III}]$ emission is extended to ~ 15 physical kpc and indicates a powerful outflow spreading over the host galaxy. The inferred ionized gas mass outflow rate is $22 \pm 3 M_{\odot} \text{ yr}^{-1}$. Although it is a radio source, according to the line diagnostics using $\text{H}\beta$, $[\text{O II}]$, and $[\text{O III}]$, photoionization by the central QSO is likely the dominant ionization mechanism rather than shocks caused by radio jets. On the other hand, the spectral energy distribution of the host galaxy is well characterized as a quiescent galaxy that has shut down star formation by several hundred Myr ago. Our results suggest a scenario that QSOs are powered after the shut-down of the star formation and help to complete the quenching of massive quiescent galaxies at high redshift.

Keywords: galaxies: evolution—galaxies: active

1. INTRODUCTION

Giant elliptical galaxies are the dominant population in clusters of galaxies today and their formation history is one of the most important issues of observational cosmology. According to their tight color-magnitude relation, they are thought to have formed the bulk of their stars in the early Universe (e.g., Bower et al. 1992; Kodama et al. 1998; Bower et al. 1998). Massive galaxies with quiescent star formation similar to giant ellipticals today have been now discovered at up to $z = 4$ (e.g., Schreiber et al. 2018; Tanaka et al. 2019; Kubo et al. 2018, 2021; Valentino et al. 2020; Forrest et al. 2020; Saracco et al. 2020). They are characterized by significant Balmer/4000Å breaks and suppressed emission in the rest-frame UV and far-infrared (FIR). According to the detailed analysis of their star formation histories (SFH) using multi-wavelength photometry and deep near-infrared (NIR) spectroscopic observations, they have likely formed via a burst of star formation quenched suddenly, and evolved passively for several hundred Myr to a few Gyr ago; however, it is not yet understood how they were quenched and how they were maintained quiescence when the Universe was still rich in gas.

Several quenching mechanisms to suppress the star formation by removing or heating gas have been adopted in cosmological numerical simulations to reproduce massive quiescent galaxies in the early Universe (e.g., Weinberger et al. 2017; Donnari et al. 2021). Active galactic nuclei (AGN) feedback is a plausible quenching mechanism (e.g., Naab & Burkert 2003; Bournaud et al. 2005; Hopkins et al. 2006; Sparre & Springel 2016) leading to a well-established relationship between the masses of the supermassive black holes (SMBH) and the bulge luminosities/masses or velocity dispersions of their host galaxies (e.g., Magorrian et al. 1998; Ferrarese & Merritt 2000; Kormendy & Ho 2013). AGN feedback is observed as quasar (radiative) mode that occurs around the peak of the AGN activity and radio (kinetic or jet) mode that occurs at a low accretion rate (Fabian 2012); strong outflows from AGNs have been observed (e.g., Rupke & Veilleux 2011; Harrison et al. 2014; Carniani et al. 2015; Harrison et al. 2016; Bae et al. 2017) while radio-loud AGNs are often hosted by giant ellipticals in the local Universe (e.g., Best et al. 2005). But it is still unclear whether AGNs have quenched the star formation; the star formation rates (SFR) of host galaxies of AGNs range widely (e.g., Santini et al. 2012; Rosario et al. 2012; Shimizu et al. 2015; Mullaney et al. 2015).

Here we present a spatially extended ionized gas outflow from a type-2 AGN in a protocluster at $z = 3.09$ detected with [O III]λλ4959,5007 emission lines. Its

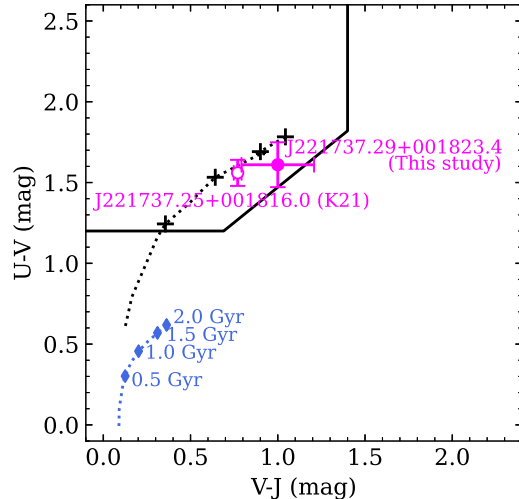


Figure 1. The rest-frame UVJ color diagram. The magenta filled circle shows the target of this study (J221737.29+001823.4) and open circle shows a massive quiescent galaxy in the same protocluster confirmed in K21 (J221737.25+001816.0). The points and curves show the color evolution tracks for SED models with age between 0.1 to 2 Gyr computed with GALAXEV (Bruzual & Charlot 2003). The black crosses with a dotted curve show the color evolution track for a single burst star formation model with $A_V = 0$. The blue diamonds and curve show the color evolution track for a constant star formation model with $A_V = 0$. The points are shown at ages 0.5, 1.0, 1.5, and 2.0 Gyr. The black solid line show the color criterion for quiescent galaxies at $2.0 < z < 3.5$ in Whitaker et al. (2013).

host galaxy is well characterized as a massive quiescent galaxy by detecting significant Balmer/4000 Å breaks photometrically. Thus the AGN in this particular object is an excellent target to understand how an AGN worked in a giant elliptical when it has been quenched star formation. This paper is organized as follows: In Section 2, we describe the target and observations. In Section 3, we describe the spectral energy distribution (SED) fitting and spectral analysis method. In Section 4, we present the result of the SED fitting and the spectral analysis. In Section 5, we discuss the properties of this QSO found in a quiescent galaxy and its powering mechanism. Section 6 summarizes our conclusions. In this study, we adopt cosmological parameters $\Omega_m = 0.3$, $\Omega_\Lambda = 0.7$ and $H_0 = 70 \text{ km s}^{-1} \text{ Mpc}^{-1}$. We assume a Chabrier (2003) Initial Mass Function (IMF). Magnitudes are expressed in the AB system. We use the vacuum rest-frame wavelengths of emission lines.

2. TARGET AND DATA

Table 1. Summary of the data

Items	References
Photometry	
CFHT MegaCam u^*	not published (PI: Cowie)
Subaru S-Cam $BVRi'z'$	Matsuda et al. (2004) Hayashino et al. (2004)
Subaru MOIRCS JHK_s	Kubo et al. (2013)
Subaru nuMOIRCS K_s	K21
<i>HST</i> ACS $F814W$	in archive (PID9760)
<i>Spitzer</i> IRAC & MIPS $24\mu\text{m}$	Webb et al. (2009)
ALMA 1.2 mm	Umehata et al. (2018)
ALMA 3.0 mm	Umehata et al. (2019)
VLA 6 GHz	Umehata et al. in prep
VLA 3 GHz	Ao et al. (2017)
VLA 1.4 GHz	Chapman et al. (2004)
<i>Chandra</i> 0.5-8 keV	Lehmer et al. (2009b)
Spectroscopy	
Subaru MOIRCS VPH- K	K15
Keck MOSFIRE H and K	Umehata et al. (2019)
VLT MUSE	Umehata et al. (2019)

2.1. Target

Table 1 summarizes the data and their reference of the target. Our target is one of the galaxies confirmed by our NIR spectroscopic observations of massive galaxies in a protocluster at $z = 3.09$ in the SSA22 field using multi-object infrared camera and spectrograph (MOIRCS; Ichikawa et al. 2006; Suzuki et al. 2008) on the Subaru telescope (Kubo et al. 2015 hereafter K15; referred J221737.3+001823.2). Hereafter we call the target as J221737.29+001823.4 adopting the source position measured on the new K_s -band image taken with updated MOIRCS (nuMOIRCS)(Kubo et al. 2021) (hereafter K21) using SExtractor (Bertin & Arnouts 1996). The source is an AGN matching with the X-ray source at 0.18 arcsec angular separation in the catalog obtained with *Chandra* in Lehmer et al. (2009a,b). Its redshift is confirmed by detecting the [O III] $\lambda\lambda 4959, 5007$ emission which shows two peaks corresponding to $z = 3.0851 \pm 0.0001$ and 3.0926 ± 0.0003 indicating complex kinematics of the ionized gas.

As we noted in K15 and revisited in section 3.1, the SED of J221737.29+001823.4 is well-fitted by a quiescent galaxy. Figure 1 shows the rest-frame UVJ color diagram to select quiescent galaxies (e.g., Whitaker et al. 2013). The UVJ colors are interpolated from the best-fit SED described in section 3.1. J221737.29+001823.4 is classified as a quiescent galaxy similar to another mas-

Table 2. Photometry

Items	Values
u^* (mag)	$> 27.2 (2\sigma)$
B (mag)	27.28 ± 0.26
V (mag)	26.77 ± 0.20
R (mag)	26.57 ± 0.18
i' (mag)	26.12 ± 0.18
z' (mag)	25.79 ± 0.21
$F814W$ (mag)	26.66 ± 0.32
J (mag)	$> 24.58 (2\sigma)$
H (mag)	$> 24.66 (2\sigma)$
K_s (mag)	22.58 ± 0.08
3.6 μm (mag)	22.15 ± 0.06
4.5 μm (mag)	21.92 ± 0.05
5.8 μm (mag)	21.86 ± 0.16
8.0 μm (mag)	21.67 ± 0.18
24 μm (μJy)	$< 100 (3\sigma)$
1.2 mm (μJy)	$< 75 (3\sigma)$
3.0 mm (μJy)	$< 43 (3\sigma)$
6 GHz (μJy)	9.56 ± 0.85
3 GHz (μJy)	13.07 ± 1.64
1.4 GHz (μJy)	$< 48 (4\sigma)$
0.5-2 keV ($\text{erg cm}^{-2} \text{ s}^{-1}$)	$1.0^{+0.6}_{-0.4} \times 10^{-16}$
2-8 keV ($\text{erg cm}^{-2} \text{ s}^{-1}$)	$11.2^{+4.3}_{-3.3} \times 10^{-16}$

sive quiescent galaxy with $z_{\text{spec}} = 3.0922^{+0.008}_{-0.004}$ at R.A., Dec = 22:17:37.25, +00:18:16.0, only 7.5 arcsec (≈ 60 in physical kpc) away from the target confirmed in K21. We note that J221737.25+001816.0 is not detected in [O III] emission and the *Chandra* and radio data described below, but shows the weak [O II] emission that can originate in an AGN. Including our studies, several studies have shown the prevalence of massive quiescent galaxies in protoclusters at up to $z = 3.37$ (e.g., Kubo et al. 2013; K21; Shi et al. 2021; McConachie et al. 2021). Such massive quiescent galaxies in protoclusters are the most plausible progenitors of typical giant ellipticals today.

In the SSA22 protocluster, AGNs have been surveyed using the *Chandra* and also *Spitzer* data (Webb et al. 2009), and those hosted by galaxies ranging from Ly α emitters to sub-mm galaxies have been studied (Webb et al. 2009; Lehmer et al. 2009a,b; Geach et al. 2009; Tamura et al. 2010; Kubo et al. 2013; K15; Umehata et al. 2015, 2019; Monson et al. 2021). Among them, J221737.29+001823.4 is not particularly luminous in X-ray but is the most [O III] luminous source observed at this point (K15).

2.2. Photometry

Table 2 summarizes the measured magnitudes and fluxes of the target. The u^* to 8.0 μm photometry was taken in the same way as K21. The u^* to K_s , and $F814W$ -band images are convolved to match the PSF to a FWHM of ≈ 1.0 arcsec, and measured fluxes with a 2.0 arcsec diameter aperture. The IRAC 3.6 – 8.0 μm photometry is applied aperture correction computed by using the K_s -band image to match with u^* to K_s -band (see detail in Kubo et al. 2013). Then we corrected the PSF matched photometries multiplying by total (Kron flux measured on nuMOIRCS image) to aperture photometry ratio in K_s -band. Major emission lines shifting to the bandpasses were checked spectroscopically and subtracted from these broadband measurements. [O II], $H\beta$ and [O III] were subtracted from the H and K -band fluxes, respectively, while $H\alpha$ and [N II] are shifted out of the bandpasses. $\text{Ly}\alpha$ and CIV were ignorable since they were observed with the Multi-Unit Spectroscopic Explorer (MUSE) on the Very Large Telescope (VLT) (Umehata et al. 2019; $2\sigma = 0.3 \times 10^{-18} \text{ erg s}^{-1} \text{ cm}^{-2} \text{ arcsec}^{-2}$) but are not detected. Type-2 AGNs show strong $\text{Ly}\alpha$ in general (e.g., Norman et al. 2002; Mignoli et al. 2019). Indeed, $\text{Ly}\alpha$ fluxes of a few $10^{-16} \text{ erg s cm}^{-2} \text{ s}^{-1}$ were detected in the narrow line AGNs at $z \sim 3$ with [O III] fluxes similar to J221737.29+001823.4 (Law et al. 2018). Although J221737.29+001823.4 itself showed no strong $\text{Ly}\alpha$, it is likely associated with the extended $\text{Ly}\alpha$ nebulae which indicate the presence of abundant intergalactic gas (Umehata et al. 2019). Thus it is natural to consider that $\text{Ly}\alpha$ photons of J221737.29+001823.4 are absorbed and/or scattered by circum/intergalactic media to form the extended $\text{Ly}\alpha$ nebulae (e.g., Hennawi et al. 2009) though the detail of $\text{Ly}\alpha$ damping mechanism is beyond the scope of this study.

J221737.29+001823.4 was observed by ALMA in the Band-6 and Band-3, which gives upper limits at 1.2 mm and 3 mm (Umehata et al. 2015, 2017, 2018, 2019). J221737.29+001823.4 was also observed by Karl G. Jansky Very Large Array (VLA) C-band (6 GHz), S-band (3 GHz; Ao et al. 2017) and L-band (1.4 GHz; Chapman et al. 2004), and is detected in 3 and 6 GHz. Here we briefly explain the recent C-band observations (details will be presented in Umehata et al. in prep). The field of view covers an entire field of ALMA deep survey field in the SSA22 (Umehata et al. 2018), which includes J221737.29+001823.4. Observations were carried out in the A and B configurations covering 4.2-8.2 GHz with a total on-source time of 89 hours. After the data reduction and imaging with VLA Common Astronomy Software Applications (CASA), the resultant map has a

synthesized beam size of $0''.89 \times 0''.79$ (PA=24.71 deg) and a rms level $0.35 \mu\text{Jy}/\text{beam}$ at the phase center. We measure the 3 GHz and 6 GHz fluxes using CASA/imfit. We also put a point-source upper limit at 1.4 GHz. We put an upper limit of *Spitzer* MIPS 24 μm (Webb et al. 2009) (see also Kubo et al. 2013). We use the *Chandra* X-ray flux values listed in Lehmer et al. (2009b). Its radio flux is around the detection limit of VLA COSMOS 3 GHz survey (Smolčić et al. 2017) and X-ray flux is lower than the detection limit of the *Chandra* COSMOS Legacy survey (Marchesi et al. 2016). To summarize, J221737.29+001823.4 is an object hardly detected by the deep and wide surveys to date.

2.3. Spectroscopy

The NIR spectroscopic observations were performed using MOIRCS (K15) and Multi-Object Spectrometer For Infra-Red Exploration (MOSFIRE; McLean et al. 2012) on Keck-I telescope (Umehata et al. 2019 and Umehata et al. in prep for details). We show the slit positions in Figure 2. The observations were conducted using three slit position angles, 5 (Slit-A), 105 (slit-B), and 58 (slit-C) degrees. For slit-A and B, we conducted a K -band spectroscopy for 3.2 and 3.3 h net exposure with MOSFIRE on 11 and 12th September 2020 (Umehata et al. 2019 and Umehata et al. in prep). For slit-A, an H -band spectrum was obtained with 2.5 h exposure with MOSFIRE on 11th September 2020 (see detail in K21). The slit widths were 0.7 arcsec for all the MOSFIRE observations. For slit-C, we conducted a K -band spectroscopy with 3.8 h exposure with MOIRCS on Subaru telescope on 29th October 2012 (K15). The location of slit-C was offset from the center of the target in order to observe the other two targets simultaneously. The slit width for the MOIRCS observation was 0.8 arcsec. All observations were conducted in good seeing conditions with FWHM PSF sizes 0.5 to 0.8 arcsec. Both MOIRCS and MOSFIRE observations were performed by 2-position mask-nod sequence dither along slits to perform sky subtraction accurately. The calibration of the fluxes was performed using one Telluric standard star at similar air masses taken before or after the observations each night. The spectral resolutions for MOSFIRE K (H) and MOIRCS K -band at the given configurations were 3620 (3660) and 1700, respectively.

Figure 2 shows the resulting spectra extracted by the MOSFIRE data reduction pipeline which is corrected of slit losses (multiplied by 1.53 to 1.98). [O II] $\lambda\lambda 3727, 3729$, $H\beta$, and [O III] are detected significantly. Although the observing methods and conditions are not uniform, the $H\beta$ and [O III] fluxes measured at each slit location do not differ greatly. In the case

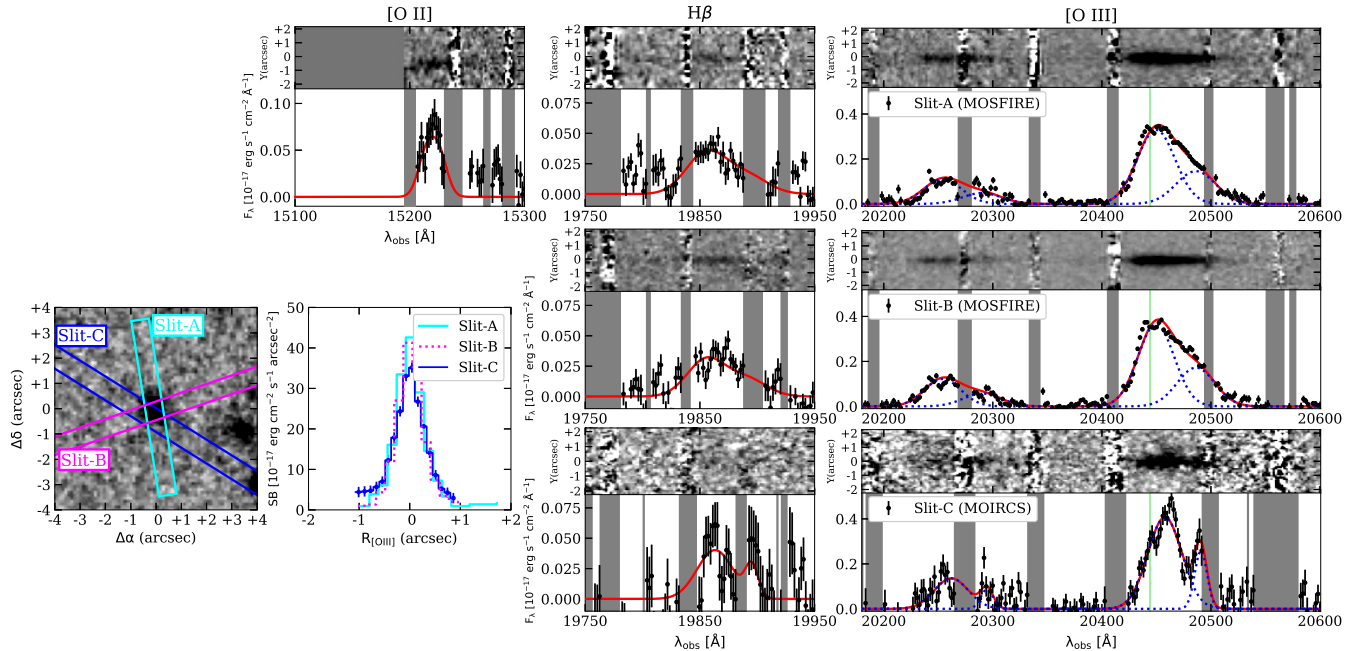


Figure 2. Bottom left: The left panel shows K_s -band image of the target. The image size is eight arcsec square. The cyan, magenta, and blue rectangles show the locations for slit-A, slit-B, and slit-C, respectively. The right panel shows the radial surface brightness profile of the [O III] emission line at each slit position. The north sides (upper side of left panel) of the slits are positive and the areas detected above 2σ are plotted. Right: The spectral images and one-dimensional spectra. The top row shows the [O II], $H\beta$ and [O III] spectra observed at slit-A. The black points are the observed spectra in which the residual sky is subtracted. The red curves show the best-fit spectra. The gray shaded regions are masked in the spectral fittings. The vertical green line shows the z_{50} of [O II] corresponding to [O III]. The middle and bottom rows from central to right are similar to the top row but show the $H\beta$ and [O III] spectra observed at slit-B and slit-C, respectively.

of J221737.25+001816.0 in K21 which was taken with the same masks as both slit-A and B, the differences between the slit loss corrected fluxes from MOSFIRE spectroscopy and the Kron fluxes based on the MOIRCS imaging in H and K_s -band were $\sim 20\%$. Thus the flux calibration in this study is almost correctly performed.

3. ANALYSIS

3.1. SED fitting

We used X-CIGALE (Yang et al. 2020), which models the SED of a host galaxy and X-ray to radio emission from an AGN simultaneously. The model parameters used in X-CIGALE are summarized in Table A1. Briefly, we included a stellar population synthesis model with dust attenuation, dust emission, an optical to infrared emission model for an AGN, X-ray power-law emission, and radio synchrotron emission. For stellar population models, we adopted a Chabrier (2003) IMF and a Bruzual & Charlot (2003) model with solar metallicity, and dust attenuation law from Calzetti et al. (2000). We assumed a delayed exponentially declining SFH model

described as,

$$\text{SFR}(t) \propto \frac{(t_o - t)}{\tau^2} \times \exp(-(t_o - t)/\tau) \text{ for } 0 \leq t \leq t_o$$

where t is the lookback-time, t_o is the lookback-time onset of star formation, and τ is the e-folding time at which the SFR peaks. We use the dust emission templates from Dale et al. (2014), which are parameterized by a power-law slope α of $dM_d(U) \propto U^{-\alpha} dU$ where M_d is the dust mass and U is the radiation field intensity and AGN fraction. The AGN fraction of this component is set to zero since we included another AGN model. X-CIGALE adopts an energy balance principle for the emission from stars, i.e., the energy emitted by dust in the IR corresponds to the energy absorbed by dust in the UV to optical.

We adopted models of rest-frame UV to IR emission from an AGN according to Fritz et al. (2006). Here we fixed the parameters at default values of X-CIGALE except for position angle (ψ) and AGN fraction. The parameters fixed here can affect the mid-IR (MIR) SED shape but this is out of the scope of this study since

the MIR flux of our target is not well constrained. The X -ray power law is parameterized by a photon index Γ . The Fritz et al. (2006) and X -ray models are constrained not to have an optical to X -ray luminosity ratio significantly different from the empirical values (Just et al. 2007). The radio synchrotron emission in X-CIGALE is parameterized with a power-law spectral slope α where radio flux $F_\nu \propto \nu^{-\alpha}$, with radio-IR correlation q_{IR} (Helou et al. 1985).

We did not include the nebular emission in X-CIGALE that is useful for modeling young star-forming galaxies but not important for a massive quiescent galaxy like our target. Our target has strong nebular emission lines from an AGN, which is not included in the AGN model templates, and their contributions to the SED were subtracted in advance. Low-mass X -ray binaries (LMXB), high mass X -ray binaries (HMXB), and hot gas from a host galaxy were also considered for the X -ray model, but according to the recipe adopted in X-CIGALE, their contribution to X -ray luminosities are expected to be two or more orders of magnitude lower than that of the AGN X -ray luminosity of our target. As shown in Figure 2, since it is hard to determine the systemic redshift of the host galaxy, hereafter we adopt $z = 3.085$ to calculate the physical properties. We also ran X-CIGALE with a fixed position angle $\psi = 0$ deg, where the contribution of the AGN is negligible at rest-frame UV to optical wavelength.

3.2. Emission lines fitting

Figure 2 shows the [O II], $H\beta$, and [O III] spectra of J221737.29+001823.4. All the [O III] line profiles have significantly redshifted tails. $H\beta$ shows no significant emission from a broad line region (FWHM > 2000 km s $^{-1}$). We measured the fluxes and line profiles of the emission lines by fitting them with combinations of Gaussian profiles. The composites of two or three Gaussian profiles are often used to fit the [O III] line profiles of AGNs (e.g., Harrison et al. 2014; Zakamska & Greene 2014). Zakamska & Greene (2014) found that three-components Gaussian models are better than two or one-component Gaussian models for 400 out of 568 obscured AGNs found in SDSS. According to Villar-Martín et al. (2011), such a three-component Gaussian model consists of two narrow components and one very broad (FWHM $\gtrsim 1000$ km s $^{-1}$) component. Such a broad component can appear as a distinct tail in a spectrum but it was not identified well in our target maybe due to the low sensitivity. As we describe in later, the line profiles of our target are approximated well by combinations of the two narrow Gaussian profiles without another very broad component. Thus to compare the line properties

properly with literatures, we fitted each [O III] by with a combination of two Gaussian components.

The line widths, central wavelengths, and intensity of the two Gaussians are free parameters. [O III] $\lambda 4959$ was fitted simultaneously with [O III] $\lambda 5007$, adopting the same model profile and a fixed line ratio [O III] $\lambda 4959$ /[O III] $\lambda 5007 = 0.33$. First, we subtracted the residual sky from each spectrum. The spectra significantly affected by OH airglow, which were automatically defined as regions where $\sigma > 1 - 5 \times 10^{-17}$ erg cm $^{-2}$ s $^{-1}$ Å $^{-1}$, were masked in advance (gray shaded in Figure 2) and not used in the fits. We then fitted the above models with MCMC using emcee (Foreman-Mackey et al. 2013) in Python. The 5th, 50th, and 95th percentiles of the samples in the marginalized distributions are quoted as means and uncertainties. The line center is defined as velocity v_{50} at which 50 percent of the line flux accumulates. The line width is defined as W_{80} , the velocity width of the line containing 80% of the total flux ($W_{80} = v_{90} - v_{10}$; see details in Harrison et al. 2014). We also measured a dimensionless relative asymmetry $= ((v_{95} - v_{50}) - (v_{50} - v_{05})) / (v_{95} - v_{05})$ (Zakamska & Greene 2014).

The fitting procedure for $H\beta$ and [O II] was similar to that of [O III], but adopted different models. $H\beta$ was fitted with the best-fit model profiles for [O III] for each slit multiplied with a free parameter. The [O II] doublet was fitted using a combination of two Gaussian profiles with the same line widths and fixed separation of the central wavelengths but with the line ratio as a free parameter. Finally, we corrected their instrumental broadening for W_{80} assuming $W_{80,\text{corr}} = [W_{80}^2 - W_{80,\text{inst}}^2]^{1/2}$ where the W_{80} is the original value obtained in the spectral fitting and $W_{80,\text{inst}}$ is W_{80} for a Gaussian with the width owed to the instrumental broadening ≈ 60 km s $^{-1}$. The corrections are less than 2% of the original values. We evaluated the spatial extent of the [O III] along the slits by taking the average spatial profiles between 20420 and 20490 Å.

Figure 2 shows the best-fit spectra and spatial extent of the [O III] emission line at each position. The red curves show the best-fit profiles. The best-fit model profiles for [O III] give reasonable fits for $H\beta$ while the observed [O II] may trace only a blue part of the [O III] as the green vertical lines in Figure 2 show the z_{50} of [O II] corresponding to the [O III].

4. RESULT

4.1. SED of the host galaxy

Figure 3 and Table 3 show the best-fit SED and parameters of J221737.29+001823.4, respectively. The AGN dominates the rest-frame UV emission. Similar

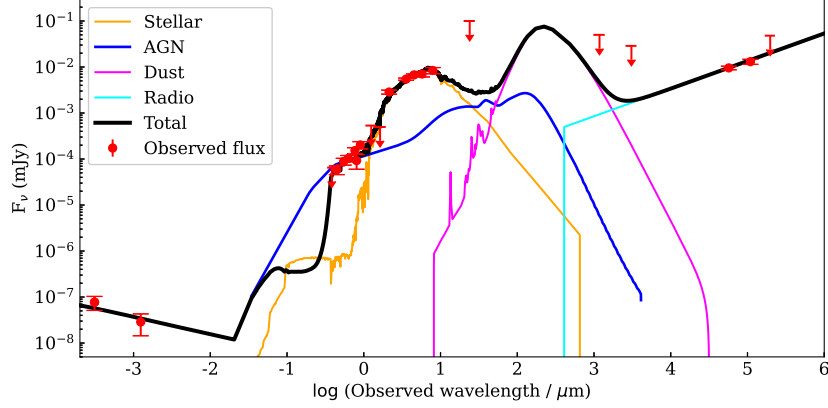


Figure 3. The best-fit SED of the target obtained with X-CIGALE. The red points show the observed fluxes with 1σ errors. The arrows show the upper limit values. The thick black curve shows the best-fit SED that is a composite of stellar emission (magenta), continuum emission from AGN (blue), dust emission (magenta), and radio synchrotron emission (cyan). The individual model components are not corrected for absorption by the intergalactic medium.

Table 3. SED parameters

Model	parameter	value (free ψ) ^a	value ($\psi = 0$) ^b
(1)	(2)	(3)	(4)
	Reduced χ^2	0.91	1.60
Stellar	age _{main} / Gyr	1.68 ± 0.29	1.40 ± 0.04
	τ_{main} / Myr	45 ± 54	200 ± 0
	$E(B - V)$ / mag	0.12 ± 0.04	0.09 ± 0.02
	age _* ^c / Gyr	1.59 ± 0.29	1.00 ± 0.36
	M_* / $10^{10} M_{\odot}$	9.91 ± 1.67	6.22 ± 0.33
	SFR / $M_{\odot} \text{ yr}^{-1}$	0.05 ± 0.02	3.41 ± 0.84
Dust	α	0.71 ± 0.70	0.14 ± 0.11
Fritz06	ψ / deg	51 ± 3	0
	f_{AGN}	0.16 ± 0.16	0.14 ± 0.14
X-ray	Γ	0.67 ± 0.20	0.65 ± 0.21
	$\log(L_{2-10\text{keV}} / \text{erg s}^{-1})$	43.2 ± 0.1	43.2 ± 0.1
Radio	q_{IR}	0.61 ± 0.28	0.61 ± 0.27
	α	0.61 ± 0.18	0.73 ± 0.22
	$\log(L_{1.4\text{GHz}} / \text{erg s}^{-1} \text{ Hz}^{-1})$	31.05 ± 0.06	31.08 ± 0.09

NOTE—^(a)The values and errors calculated with X-CIGALE.

^(b)Calculated with a fixed position angle $\psi = 0$ deg.

^(c)The stellar mass weighted age.

Table 4. Detected emission lines

Slit	line	z_{50}	$W_{80,corr}$ (km s^{-1})	Rel. asym.	Flux ($10^{-17} \text{ erg cm}^{-2} \text{ s}^{-1}$)	$[\text{OII}]\lambda 3727/\lambda 3729$
(1)	(2)	(3)	(4)	(5)	(6)	(7)
A	$[\text{OIII}]\lambda 5007$	$3.0850^{+0.0002}_{-0.0002}$	1174^{+133}_{-50}	$0.14^{+0.03}_{-0.03}$	$21.0^{+0.8}_{-0.8}$...
	$\text{H}\beta$				$2.2^{+0.2}_{-0.2}$...
B	$[\text{OII}]\lambda\lambda 3727, 3729$	$3.0821^{+0.0012}_{-0.0010}$	354^{+128}_{-128}		$1.4^{+0.3}_{-0.3}$	$1.0^{+1.8}_{-0.3}$
	$[\text{OIII}]\lambda 5007$	$3.0851^{+0.0002}_{-0.0002}$	1148^{+140}_{-47}	$0.15^{+0.04}_{-0.03}$	$22.7^{+0.9}_{-0.9}$...
C	$\text{H}\beta$				$2.0^{+0.2}_{-0.2}$...
	$[\text{OIII}]\lambda 5007$	$3.0857^{+0.0006}_{-0.0005}$	903^{+254}_{-91}	$0.07^{+0.11}_{-0.07}$	$19.9^{+2.6}_{-2.1}$...
	$\text{H}\beta$				$2.0^{+0.5}_{-0.5}$...

Table 5. The [O III] line profile

Slit	z	V_{offset}^a (km s $^{-1}$)	$\text{FWHM}_{\text{corr}}$ (km s $^{-1}$)	fraction b
(1)	(2)	(3)	(4)	(5)
A	$3.0832^{+0.0002}_{-0.0001}$...	242^{+24}_{-17}	$0.68^{+0.04}_{-0.06}$
	$3.0905^{+0.0005}_{-0.0036}$	533^{+36}_{-265}	253^{+83}_{-24}	$0.32^{+0.06}_{-0.04}$
B	$3.0832^{+0.0002}_{-0.0001}$...	229^{+25}_{-17}	$0.67^{+0.04}_{-0.07}$
	$3.0905^{+0.0005}_{-0.0027}$	535^{+32}_{-245}	240^{+79}_{-21}	$0.33^{+0.07}_{-0.04}$
C	$3.0848^{+0.0005}_{-0.0005}$...	147^{+69}_{-54}	$0.81^{+0.08}_{-0.22}$
	$3.0914^{+0.0009}_{-0.0037}$	484^{+73}_{-247}	$\lesssim 180$	$0.19^{+0.21}_{-0.08}$

NOTE—^(a) The velocity offset of this component from the brighter component.

^(b) The fraction of this component in the total flux.

to our previous SED modeling without an AGN component (K15), the best-fit SED is that of a massive quiescent galaxy but due to the contribution of the AGN to the rest-frame UV, old stars are more dominant where the best-fit age and stellar mass become larger. The reduced χ^2 value for the $\psi = 0$ model is larger than that for the ψ free model but still, the $\psi = 0$ model can fit the observed fluxes well. Therefore, we cannot reject the possibility that J221737.29+001823.4 has a smaller ψ in fact and the AGN contribution on the SED at rest-frame UV is overestimated.

The best-fit SED from X-CIGALE at IR is lower than the upper limit of the observed fluxes. Adopting the average 1.2 mm flux to IR luminosity L_{IR} relation for the SED library in Danielson et al. (2017), the conservative upper limit of L_{IR} is $\sim 0.9 - 2.0 \times 10^{11} L_{\odot}$ taking the 95% confidence interval. It corresponds to $\text{SFR} < 9 - 21 M_{\odot} \text{ yr}^{-1}$ using the L_{IR} to SFR conversion in Kennicutt & Evans (2012). Hereafter we use $L_{\text{IR}} = 2.0 \times 10^{11} L_{\odot}$ and $\text{SFR} = 21 M_{\odot} \text{ yr}^{-1}$ to estimate a conservative upper limit.

4.2. AGN luminosity

Table 4 lists the strength, line center and line width at each slit position. Using the largest flux value at slit-B, J221737.29+001823.4 has a [O III] luminosity of $\log(L_{[\text{OIII}]} / \text{erg s}^{-1}) = 43.28 \pm 0.01$. The observed X -ray luminosity is $\log(L_{2-10\text{keV}} / \text{erg s}^{-1}) = 43.2 \pm 0.1$. Thus $L_{[\text{OIII}]}$ is more than ten times larger than that expected from the empirical X -ray to [O III] luminosity relation for type-1 AGNs in the local Universe (e.g., Ueda et al. 2015). Furthermore, our target has a flat X -ray SED ($\Gamma = 0.67 \pm 0.20$) that suggests significant

absorption on X -ray where $\Gamma \sim 1.8$ in typical (e.g., Yang et al. 2016; Liu et al. 2017). We then estimated the intrinsic X -ray luminosity based on the [O III] luminosity. Adopting the X -ray to [O III] luminosity relation for Seyfert-1 AGNs in the local Universe (Ueda et al. 2015), J221737.29+001823.4 has an intrinsic X -ray luminosity of $\log(L_{2-10\text{keV, intrinsic}} / \text{erg s}^{-1}) \approx 44.4$. Applying the X -ray to bolometric correction as in Marconi et al. (2004), the source has a bolometric luminosity of $\log(L_{\text{bol}} / \text{erg s}^{-1}) \approx 46.0$, which would make it a moderately luminous QSO. Assuming a scaling relation between the black hole mass and the host galaxy stellar mass of $M_{\text{BH}} \approx 0.002 M_{*}$, following Aird et al. (2012), J221737.29+001823.4 may have $M_{\text{BH}} \approx 2 \times 10^8 M_{\odot}$ and Eddington luminosity $L_{\text{Edd}} = 1.3 \times 10^{38} M_{\text{BH}} / M_{\odot} \approx 2.6 \times 10^{46} \text{ erg s}^{-1}$. Thus it may have a relatively large Eddington ratio of $L_{\text{bol}} / L_{\text{Edd}} \sim 0.4$.

4.3. Radio emission

J221737.29+001823.4 has a radio spectral index $\alpha = 0.61 \pm 0.18$ where $F_{\nu} \propto \nu^{-\alpha}$, which is a typical value of radio synchrotron emission (e.g., Smolčić et al. 2017). The luminosity at 1.4 GHz is given as $L_{1.4\text{GHz}} = F_{1.4\text{GHz}} 4\pi D_L^2 (1+z)^{(\alpha-1)}$ where D_L is a luminosity distance, and $F_{1.4\text{GHz}}$ is the flux at 1.4 GHz, which is $0.021 \pm 0.003 \text{ mJy}$ from X-CIGALE. Then we find a radio luminosity of $\log(L_{1.4\text{GHz}} / \text{erg s}^{-1} \text{ Hz}^{-1}) = 31.05 \pm 0.06$. It would be classified as a radio-quiet AGN adopting the criteria suggested by Xu et al. (1999). The logarithmic ratio of the infrared and radio fluxes q_{IR} of J221737.29+001823.4 is 0.61 ± 0.28 for the best-fit model of X-CIGALE where q_{IR} is defined as $\log_{10}(F_{\text{FIR}} / (3.75 \times 10^{12} \text{ Hz}) / F_{1.4\text{GHz}})$ (Helou et al. 1985). Using a conservative upper limit on L_{IR} , q_{IR} is $\lesssim 1.4$. It is lower than that of pure star-forming galaxies with 2.4 in Ivison et al. (2010) and comparable to radio-loud AGNs at low redshift (e.g., Toba et al. 2019). At high redshift, QSOs selectable by wide-field surveys like SDSS have q_{IR} similar to star-forming galaxies (Ibar et al. 2008; Murphy 2009) while radio sources with low q_{IR} like local radio-loud AGNs are found by deep surveys like VLA COSMOS 3 GHz survey (Delhaize et al. 2017). Thus J221737.29+001823.4 is one of the most local radio-loud AGN-like objects selectable by the radio surveys to date.

Figure 4 shows the 6 GHz image and the flux contours of the radio emission overlaid on the K_s -band image. J221737.29+001823.4 is well resolved at 6 GHz where the image component size after deconvolution of the beam are $(0.99 \pm 0.05) \times (0.52 \pm 0.05) \text{ arcsec}$ and $\text{PA} = 151.2 \pm 4.6 \text{ deg}$. There is also a diffuse component with an orientation different from that of the bright central source. The source lies at the low power end of

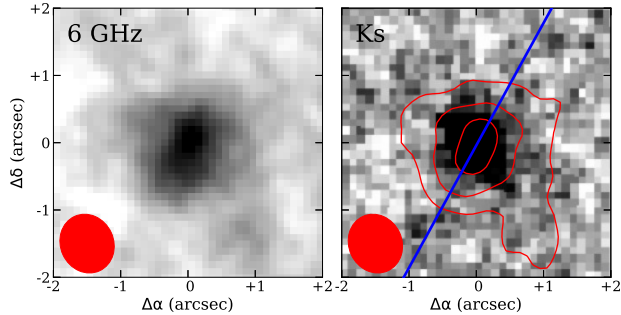


Figure 4. Left: The 6 GHz image of the target. The image size is 4 arcsec by side. The red filled ellipse shows the beam size at 6 GHz. Right: The 3, 6, and 9 σ contours (red) of the 6 GHz are overlaid on the K_s -band image of the target. The blue line shows the position angle measured at 6 GHz.

the distribution for compact steep spectrum radio galaxies (e.g., Gelderman & Whittle 1994; O’Dea 1998) that are believed to be young systems evolving into more extended radio galaxies or the systems prevented the spatial growths by the dense interstellar medium (ISM). The radio position angle is different from the slit directions for NIR spectroscopy and then it is not clear whether the [O III] traces the radio morphology. But the similar spatial extents of [O III] and radio emission can indicate their physical connection though both are limited by the observational depths.

4.4. Outflow

Although the small notches of the spectra left from the model spectra indicate further more complex kinematics, each spectrum is well approximated by a combination of two Gaussian profiles. The obtained spectra have large relative asymmetries 0.07 – 0.15 and line widths of $\approx 1000 \text{ km s}^{-1}$. The spatial extent of [O III] ($\approx 15 \text{ kpc}$ in Figure 2) of J221737.29 +001823.4 is much larger than the typical size of a massive quiescent galaxy at high redshift (a few physical kpc; e.g., Shibuya et al. 2015) though the size of the host galaxy cannot be evaluated robustly since the K_s -band image can be significantly contaminated by [O III] emission. These line profiles observed at each slit indicate a significant outflow of ionized gas spread over the host galaxy. Such galactic wide-scale outflows of ionized gas have been observed among AGNs in the local Universe and at high redshift (e.g., Harrison et al. 2014; Genzel et al. 2014; Harrison et al. 2016; Law et al. 2018; Kakkad et al. 2020).

Table 4 summarizes the ingredient of each spectrum. At all slit locations, a spectrum consists of two narrow components. The redshift of the bluer components at slit-A and B match with that of [O II] within errors

while the redshifts of both the two components at slit-C are redder than [O II]. Therefore, J221737.29 +001823.4 consists of one component also detected with [O II] at $z \approx 3.0832$ (i), and at least two redshifted components (ii. bluer component at slit-C, and iii. redder components at slit-A, B and C, at the resolution of this study). Comparing with local AGNs with [O III] line width as wide as J221737.29 +001823.4 in literature (Villar-Martín et al. 2011; Fu et al. 2012; Zakamska & Greene 2014), J221737.29 +001823.4 has components with narrower line width and a larger velocity offset between the first and second brightest components. Then the wide line widths of the whole line profiles of J221737.29 +001823.4 are due to the large velocity offsets of the two components while those are due to broad components for most of the type-2 AGNs. The broader components found in such type-2 AGNs are generally blueshifted from the narrower components and regarded as highly disturbed outflowing gas. In the case of J221737.29 +001823.4, the component-(iii) seen at all slit positions likely comes from the gas near the central SMBH. Since the emission lines are spatially extended at all slit directions, component-(i) and (iii) which dominate the emission-line fluxes at slit-A and B, and slit-C, respectively, likely come from the outflowing extended emission-line region. The narrower line width indicates that the outflowing gas is not highly perturbed like typical type-2 AGNs with wide line width. Maybe the outflowing gas of this system is not disturbed because of young age, lack of intergalactic gas to interact, or the wing of the gas is highly attenuated by dust.

Here we estimate the mass outflow rate of J221737.29 +001823.4 following Fiore et al. (2017), using the [O III] $W_{80,corr}$ and the spatial extent and $H\beta$ luminosity for slit-A which are similar to those for slit-B and slit-C. Based on the $H\beta$ luminosity, the mass of the outflowing ionized gas is estimated as

$$M_{H\beta} = 7.8 \times 10^8 C \left(\frac{L_{H\beta}}{10^{44}} \right) \left(\frac{\langle n_e \rangle}{10^3} \right)^{-1},$$

following Osterbrock & Ferland (2006) and Carniani et al. (2015), where $C = \langle n_e \rangle^2 / \langle n_e^2 \rangle$ (set to unity which is a conservative lower limit) and a gas temperature $T = 10^4 \text{ K}$ is assumed. Adopting $n_e = 200 \text{ cm}^{-3}$ following Fiore et al. (2017), we find $M_{H\beta} = 7.2^{+0.7}_{-0.7} \times 10^7 M_{\odot}$.

The mass outflow rate of ionized gas is calculated as,

$$\dot{M} = 3 \times v_{max} \times M_{H\beta} / R,$$

where v_{max} is the wind maximum velocity, and R is the radius at which the mass outflow rate is computed. v_{max} is defined as $W_{80,corr}/1.3$ and R is defined as the

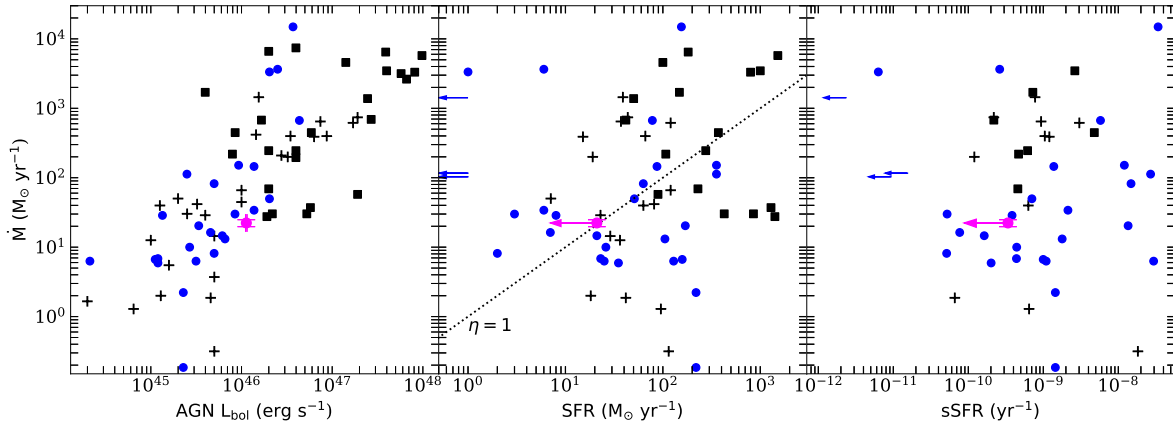


Figure 5. Mass outflow rate vs. AGN bolometric luminosity L_{bol} (left), and SFR (center) and sSFR (right) of the host galaxy. The filled magenta circle shows J221737.29+001823.4. The black crosses and filled squares show the QSOs at low and high redshift from [Fiore et al. \(2017\)](#). The blue-filled circles show AGNs in [Leung et al. \(2019\)](#). We corrects the mass outflow rate in [Leung et al. \(2019\)](#) adopting the equation in [Fiore et al. \(2017\)](#). The dashed line in the central panel shows $\eta = 1$.

maximum radius at which the high velocity gas is detected. Here we use half of the extent of [O III] for each slit, ≈ 7.1 kpc, corrected of the spatial resolution with FWHM PSF of ≈ 4.5 kpc on average. We find a mass outflow rate $22 \pm 3 M_{\odot} \text{ yr}^{-1}$. Its mass loading factor $\eta = \dot{M}/\text{SFR}$ is higher than unity, or the \dot{M} exceeds the SFR. Note that our estimate does not include outflowing gas at a neutral or molecular state. Including them, the total mass outflow rate and thus η could be a few to ten times larger than that of the ionized gas (e.g., [Rupke & Veilleux 2013](#); [Carniani et al. 2015](#); [Fiore et al. 2017](#); [Fluetsch et al. 2019](#)).

We compared the mass outflow rate, AGN bolometric luminosity, SFR, and specific SFR (sSFR) of J221737.29+001823.4 with results in [Fiore et al. \(2017\)](#) who summarized outflow properties of QSOs at low and high redshift in the literature, and [Leung et al. \(2019\)](#) who investigated outflow properties for X -ray AGNs at $1.4 < z < 3.8$ in Figure 5. We used the upper limit on SFR from the 1.2 mm flux ($< 21 M_{\odot} \text{ yr}^{-1}$) and the stellar mass estimated assuming $\psi = 0$ to obtain sSFR as a conservative limit. J221737.29+001823.4 is not a special object; its ionized gas mass outflow rate is similar to those of AGNs with similar bolometric luminosities. As previous studies have shown, the SFRs of AGNs with strong outflows range widely from quiescent (sSFR $< 10^{-10} \text{ yr}^{-1}$) to starbursting.

4.5. Emission line diagnostics

We show the emission line diagnostics of J221737.29+001823.4 measured at slit-A in Figure 6. The left panel shows O32 vs. R23, where O32 and R23 are defined

as $\log([\text{O III}]/[\text{O II}])$ and $\log(([\text{O III}]+[\text{O II}])/H\beta)$, respectively. The right panel shows $[\text{O III}]\lambda 5007/H\beta$ vs. $[\text{O II}]\lambda\lambda 3726,3729/H\beta$ line diagnostics. The magenta filled circle shows the line ratio of J221737.29+001823.4. The blue and red diamonds show the line ratios of the bluer and redder components. The black filled contour and blue contour show star-forming galaxies and AGNs, respectively, selected from Sloan digital sky survey (SDSS) using spectroscopic data products from the Max Planck Institute for Astrophysics and Johns Hopkins University DR8 catalog (MPA-JHU, [Brinchmann et al. 2004](#); [Kauffmann et al. 2004](#); [Tremonti et al. 2004](#)). The star-forming galaxies and AGNs are classified using BPT diagrams ([Baldwin et al. 1981](#)) following [Kewley et al. \(2006\)](#). We applied extinction correction using the $H\alpha/H\beta$ line ratio adopting the [Cardelli et al. \(1989\) extinction law for SDSS while no extinction correction was applied for our target.](#)

J221737.29+001823.4 has large O32 and $[\text{O III}]\lambda 5007/H\beta$ indices and is at the edge of the distribution of local AGNs. Such line ratios are seen among young star-forming galaxies with high ionization parameters at $z = 2 \sim 3$ ([Strom et al. 2018](#)) while AGN is plausibly the dominant ionizing source for our target given the low SFR and the evolved stellar population. [Law et al. \(2018\)](#) finds similarly high $[\text{O III}]\lambda 5007/H\beta$ for the optically faint ($R = 20 - 25$) AGNs at $z \sim 2 - 3$ and they are certainly classified as AGNs using BPT diagram.

We compare the line ratios with models of photoionization by AGNs ([Groves et al. 2004](#)) and shock excitation by outflows ([Allen et al. 2008](#)). [Groves et al. \(2004\)](#) provides line intensities predicted for dusty and radi-

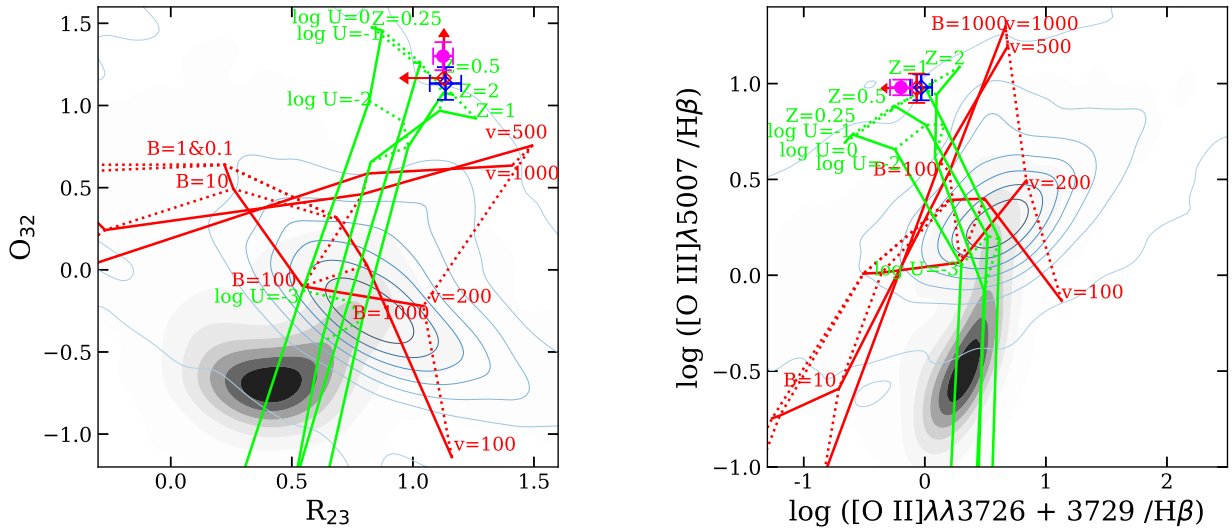


Figure 6. *Left:* O32 vs. R23 indices. The filled magenta circle with error bars shows the target. The filled black contour shows the distribution of star-forming galaxies from SDSS (based on MPA-JHU catalog; Brinchmann et al. 2004; Kauffmann et al. 2004; Tremonti et al. 2004). The blue contour shows the distribution of AGNs selected from SDSS. Both the star-forming galaxies and AGNs are selected based on BPT diagram. The green tracks show the photoionization model from Groves et al. (2004). The models with $\alpha = -2$, $\log U = -4, -3, -2, -1, 0$, and $Z = 0.25, 0.5, 1, \& 2 Z_{\odot}$ are shown. The red tracks show the shock ionization model from Allen et al. (2008). The models with $n = 1000 \text{ cm}^{-3}$, $Z = Z_{\odot}$, $v = 100, 250, 500, \& 1000 \text{ km s}^{-1}$, and $B = 0.1, 10, 100, \& 1000 \mu\text{G}$ are shown. *Right:* Similar to the left panel but for $[\text{O III}]\lambda 5007/\text{H}\beta$ vs. $[\text{O II}]\lambda\lambda 3726 + 3729/\text{H}\beta$ line diagnostics.

ation pressure dominated photoionization models using MAPPING III code (Sutherland & Dopita 1993). It describes the intensities of the emission lines from the narrow line region (NLR) of AGNs with power law ionizing SED with hydrogen density $n_{\text{H}} = 1000 \text{ cm}^{-3}$, $\alpha = -1.2$ to -2.0 , ionization parameter $\log U = -4$ to 0 , and metallicity $Z = 0.25$ to $2 Z_{\odot}$. Here we show the dusty model in Groves et al. (2004) with $\alpha = -2$, $\log U = -4$ to 0 , and $Z = 0.25$ to $2 Z_{\odot}$. Allen et al. (2008) also uses MAPPING III but provides line intensities predicted for shock excitation. They provide models with preshock density $n = 0.01$ to 1000 cm^{-3} , velocity $v < 1000 \text{ km s}^{-1}$, magnetic field $B = 10^{-10}$ to 10^{-4} G , and magnetic parameter $B/n^{1/2} = 10^{-4}$ to $100 \mu\text{G cm}^{3/2}$. We show the models with $n = 1000 \text{ cm}^{-3}$, $v = 100$ to 1000 km s^{-1} , and $B = 0.1$ to $1000 \mu\text{G}$. We choose $\alpha = -2$ and $n = 1000 \text{ cm}^{-3}$ models since only these models have line ratios close to our target.

The line ratios of J221737.29+001823.4 are close to those of the photoionization models with high ionization parameter $\log U > -1$. It indicates that most of its emission originates in the central AGN rather than the shock induced by e.g., radio jets. The line ratios of individual velocity components are also consistent

with the photoionization models. Thus the outflowing gas of J221737.29+001823.4 is likely ionized by the central AGN rather than shock excitation. It is consistent with the spatially resolved spectroscopic analysis in e.g., Fischer et al. (2017); Revalski et al. (2018) for local AGNs. We note that there are several known uncertainties in our results. First, the line ratio based on the slit spectroscopy can be a composite of several independent components. For a more detailed discussion, we need a spatially resolved spectroscopy. Second, the dust attenuation is not corrected for our target but is negligible assuming the absorption on emission lines $E(B - V)_{\text{line}} = E(B - V)/0.44 \approx 0.2$ measured with X-CIGALE; R23 and $[\text{O III}]/\text{H}\beta$ do not change significantly while O32 can decrease with ~ 0.1 and $\log([\text{O II}]/\text{H}\beta)$ can increase with ~ 0.1 adopting Cardelli et al. (1989) extinction law.

We can also measure the electron density (n_e) using the $[\text{O II}]\lambda 3727$ to $\lambda 3729$ line ratio (Osterbrock & Ferland 2006). Following Sanders et al. (2016), the line ratio of our target corresponds to an electron density $n_e = 10 - 1500 \text{ cm}^{-3}$, which is within the expected range for NLR, $10 - 10000 \text{ cm}^{-3}$ (e.g., Nesvadba et al. 2006; Liu et al. 2013).

5. DISCUSSION

We identified a QSO in a quiescent galaxy that plausibly stopped star formation several hundred Myr ago which is analogous to so-called post-starburst galaxies selected with Balmer absorption features caused by A-type stars in the local Universe though our target is hardly detected of Balmer absorption features with the current facilities. Post-starburst galaxies often show significant emission lines those likely originated in AGN rather than star formation (e.g., Yan et al. 2006; Schawinski et al. 2007; Wild et al. 2010; Alatalo et al. 2016). Similarly, massive quiescent galaxies at high redshift sometimes show weak [OII] or [OIII] which are thought to originate in AGNs (e.g., Lemaux et al. 2010; Schreiber et al. 2018; Saracco et al. 2020; K21). However, the QSOs with [O III] as luminous as our target are rarely found in the local Universe (Jarvis et al. 2019). The QSOs hosted by quiescent galaxies at high redshift have not been studied in detail previously, but they may not be so unusual given the presence of QSOs with low sSFR and strong outflows (e.g., Fiore et al. 2017; Leung et al. 2019).

In the case of J221737.29+001823.4, photoionization by AGN is likely the dominant excitation mechanism but shocks can also be the dominant excitation mechanism of strong emission lines of post-starburst galaxies (Alatalo et al. 2016). The type-2 QSOs with broad and luminous [O III] at $z < 0.2$ in Harrison et al. (2014) support the shock excitation scenario though they share several properties with J221737.29+001823.4; they have $\log(L_{[\text{OIII}]}) / \text{erg s}^{-1} = 42 - 43.2$, [O III] line FWHM = 800 – 1800 km s⁻¹, $\log(L_{1.4\text{GHz}} / \text{W erg}^{-1} \text{s}^{-1}) = 30.3 - 31.4$, compact radio sizes (1-25 kpc), small $q_{\text{IR}} = 1 - 2$, and low SFR of $\lesssim 50 M_{\odot} \text{ yr}^{-1}$, and thus are classified as radio-quiet QSOs. Jarvis et al. (2019) suggested a scenario in which low-power radio jets are confined by the ISM for a long time and efficiently affect the ISM over a large volume and result in strongly ionized gas outflows (e.g., Mukherjee et al. 2016).

How to power a QSO in a quiescent galaxy like J221737.29+001823.4? Since radio-quiet QSOs are generally star-forming (e.g., Best & Heckman 2012; Panessa et al. 2019), it is not surprising that there is abundant gas to fuel central SMBHs. However, J221737.29+001823.4 has likely been quenched for several hundred Myr. One interesting issue is the origin of the gas supply to power a QSO. Since J221737.29+001823.4 is at high redshift, cold gas supply can be still abundant though star formation should be kept quenching according to the observed SED.

Another possible supply of gas to power a QSO is mass loss from evolved stars following a starburst (Norman

& Scoville 1988; Ciotti & Ostriker 2007; Kauffmann & Heckman 2009). In this scenario, the mass loss from asymptotic giant branch (AGB) stars can result in a rise of AGN at 100 ~ 300 Myr after the starburst and may explain some observed time-delay of AGNs found in the local Universe (e.g., Davies et al. 2007; Kauffmann & Heckman 2009; Wild et al. 2010). In this scenario, the mass loss from supernova explosions (SNe) supplies gas at early times during which the mass accretion to central SMBHs is not efficient because the velocity of the gas ejected by SNe is several thousand km s⁻¹. At late times, mass loss from AGB stars becomes dominant. Since the speed of the gas ejected as planetary nebulae is several ten km s⁻¹, they can more easily accrete into the central SMBH.

Since the SFH of massive quiescent galaxies at high redshift is believed to be more bursty than the local star-forming galaxies (e.g., Schreiber et al. 2018; Kubo et al. 2021; Forrest et al. 2020; Valentino et al. 2020; Saracco et al. 2020), after the starburst, a large amount of gas should be supplied from evolved stars in a short timescale. We calculated the gas production from the mass loss of stars in J221737.29 +001823.4 using GALAXEV (Bruzual & Charlot 2003) assuming a constant starburst for 50 Myr which forms a stellar mass of $5 \times 10^{10} M_{\odot}$ or half the stellar mass of J221737.29 +001823.4 where the lifetime of SMGs are found 40–200 Myr (Greve et al. 2005; Tacconi et al. 2006; Toft et al. 2014). There is a supply of $\gtrsim 10 M_{\odot} \text{ yr}^{-1}$ gas from mass loss of stars at all times within ~ 1 Gyr from the beginning of the starburst. Using the equation adopted by Wild et al. (2010), the black hole accretion rate (BHAR) of our target is estimated from the [O III] luminosity as $4 \times 10^{-10} \times L_{[\text{OIII}]} / L_{\odot} \approx 2 M_{\odot} \text{ yr}^{-1}$ that is reduced if a part of [O III] is induced by radio jets. It is the 20 % of the mass loss from stars expected for J221737.29 +001823.4. We note that Ciotti et al. (2010) predicted that 2% of the recycled gas is used to fuel the central SMBH. From the above, a substantial amount of AGN luminosity can be fueled naturally by mass loss from stars but we cannot reject the possibility of an external supply of the gas from the circum/intergalactic media to fuel the central SMBH.

6. CONCLUSION

We have identified a massive quiescent galaxy hosting a QSO with ionized gas outflows by detecting redshifted [O III] $\lambda\lambda 4959, 5007$ emission lines. Large line widths ($W_{80} > 1000 \text{ km s}^{-1}$) measured at the three slit positions indicate the presence of powerful outflow in multiple directions. Given the quiescent SED of the host galaxy, we conclude that we are witnessing a QSO arising sev-

eral hundred Myr after the quenching of the starburst. According to the emission line diagnostics, most of the emission line flux is likely results from radiative heating by the QSO rather than radio jets.

Our results suggest a new aspect of the role of AGNs in galaxy evolution at high redshift. In one popular galaxy and SMBH co-evolution scenario, it is believed that a central SMBH is grown with the star formation of a host galaxy, QSO-driven outflows remove gas from a host galaxy and quench its star formation, after which the accretion rates onto the central SMBHs decline and radio jets regulate the star formation of a host galaxy. Indeed there are dusty starburst galaxies and obscured AGNs which are believed to be the previous steps of QSOs in this $z = 3.09$ protocluster. On the other hand, in this case, we find that a QSO appears several hundred Myr after the quenching of star formation. The presence of powerful outflow suggests that there remains a significant supply of gas to power a QSO after quenching. Taken together, it is possible that the progenitors of giant ellipticals may become strong QSOs both before and after quenching. We suggest a scenario in which once a QSO and/or stellar feedback initially quenches star formation, subsequent accretion onto the SMBH of residual gas can power a QSO effectively, and this late-time QSO further completes a quenching.

ACKNOWLEDGMENTS

This work has been supported by JSPS KAKENHI Grant Numbers 20K14530, 21H044902 (MK), 17K14252, 20H01953 (HU), 19H00697, 20H01949 (TN), 17H06130 (YT and KK). This work has been also supported by a US National Science Foundation (NSF) grant AST-2009278 (CCS). This work has been also supported by NAOJ ALMA Scientific Research Grant Numbers 2018-09B (YT) The spectroscopic data were obtained at the W. M. Keck Observatory, which is operated as a scientific partnership among the California Institute of Technology, the University of California, and the National Aeronautics and Space Administration. The observations were carried out within the framework of Subaru-Keck/Subaru-Gemini time exchange program which is operated by the National Astronomical Observatory of Japan. The K_s -band image was collected with nuMOIRCS at Subaru Telescope, which is operated by the National Astronomical Observatory of Japan. We are honored and grateful for the opportunity of observing the Universe from Maunakea, which has the cultural, historical, and natural significance in Hawaii. This paper makes use of the following ALMA data: ADS/JAO.ALMA#2013.1.00162.S, ADS/JAO.ALMA#2016.1.00580.S, ADS/JAO.ALMA#2017.1.01332.S. ALMA is a partnership of ESO (representing its member states), NSF (USA), and NINS (Japan), together with NRC (Canada), MOST and ASIAA (Taiwan), and KASI (Republic of Korea), in cooperation with the Republic of Chile. The Joint ALMA Observatory is operated by ESO, AUI/NRAO, and NAOJ. The $F814W$ -band image is based on observations made with the NASA/ESA Hubble Space Telescope, obtained from the data archive at the Space Telescope Science Institute. STScI is operated by the Association of Universities for Research in Astronomy, Inc. under NASA contract NAS 5-26555. The National Radio Astronomy Observatory is a facility of the National Science Foundation operated under cooperative agreement by Associated Universities, Inc.

APPENDIX

A. X-CIGALE PARAMETER

Table A1 lists the parameters adopted in X-CIGALE. The details of the parameters are described in Yang et al. (2020).

REFERENCES

- Aird, J., Coil, A. L., Moustakas, J., et al. 2012, ApJ, 746, 90. doi:10.1088/0004-637X/746/1/90
- Alatalo, K., Cales, S. L., Rich, J. A., et al. 2016, ApJS, 224, 38. doi:10.3847/0067-0049/224/2/38

Table 1. Range of X-CIGALE model parameters

Component	Model
(1)	(2)
SFH	sfhdelayed model without no additional burst. $\tau_{\text{main}} = 5, 10, 20, 50, 100, 200, 500, \& 1000$ Myr, $\text{age}_{\text{main}} = 0.4$ to 2.2 with 0.2 Gyr steps.
stellar population	Bruzual & Charlot (2003) SSP model, Chabrier (2003) IMF, and solar metallicity
dust attenuation	The modified Calzetti et al. (2000) attenuation model. $E(B - V)_{\text{lines}} = 0$ to 1 with 0.2 steps. $E(B - V)$ of stellar continuum is 0.44 times the $E(B - V)_{\text{lines}}$.
dust emission	Dale et al. (2014) dust emission model. $\alpha = 0.0625, 0.2500, 1.0000, \& 2.0000$. The AGN fraction of this component is set to zero.
nebular emission	None
AGN (Fritz06)	Fritz et al. (2006) model. $r_{\text{ratio}} = 60.0$, $\tau = 1.0$, $\Gamma = 0.0$, opening_angle of the dust torus = 100, angle between equatorial axis and line of sight (ψ) = 0.001 to 60.100 with 10 deg steps (= 90 for type-1 and 0 for type-2), AGN fraction = 0.0 to 1.0 with 0.1 steps, The extinction law of polar dust is Calzetti et al. (2000), $E(B-V)$ for extinction in polar direction = 0.2, 0.4, & 0.6, temperature of the polar dust = 100 K, and emissivity index of the polar dust = 1.6.
X-ray	AGN photon index $\Gamma = 0.4$ to 2.0 with 0.2 steps, maximum deviation of α_{ox} from the empirical relation = 0.2, The photon indices of LMXB and HMXB are 1.56 and 2.0, respectively.
radio	Power law slope $\alpha = 0.4, 0.6, 0.8, \& 1.0$, radio-IR correlation $q_{\text{IR}} = 0.01, 0.1, 0.3, 0.5, 1.0, \& 2.5$.
free parameters	τ_{main} , age_{main} , and $E(B - V)_{\text{lines}}$ for stellar population. AGN fraction and ψ for AGN (Fritz06) model. Γ for AGN (X-ray) model. α and q_{IR} for radio model. Thus free parameters are eight in total.

Allen, M. G., Groves, B. A., Dopita, M. A., et al. 2008, ApJS, 178, 20. doi:10.1086/589652

Ao, Y., Matsuda, Y., Henkel, C., et al. 2017, ApJ, 850, 178. doi:10.3847/1538-4357/aa960f

Bae, H.-J., Woo, J.-H., Karouzos, M., et al. 2017, ApJ, 837, 91. doi:10.3847/1538-4357/aa5f5c

Baldwin, J. A., Phillips, M. M., & Terlevich, R. 1981, PASP, 93, 5. doi:10.1086/130766

Bertin, E. & Arnouts, S. 1996, A&AS, 117, 393. doi:10.1051/aas:1996164

Best, P. N., Kauffmann, G., Heckman, T. M., et al. 2005, MNRAS, 362, 25. doi:10.1111/j.1365-2966.2005.09192.x

Best, P. N. & Heckman, T. M. 2012, MNRAS, 421, 1569. doi:10.1111/j.1365-2966.2012.20414.x

Bournaud, F., Jog, C. J., & Combes, F. 2005, A&A, 437, 69. doi:10.1051/0004-6361:20042036

Bower, R. G., Lucey, J. R., & Ellis, R. S. 1992, MNRAS, 254, 601. doi:10.1093/mnras/254.4.601

Bower, R. G., Kodama, T., & Terlevich, A. 1998, MNRAS, 299, 1193. doi:10.1046/j.1365-8711.1998.01868.x

Brinchmann, J., Charlot, S., White, S. D. M., et al. 2004, MNRAS, 351, 1151. doi:10.1111/j.1365-2966.2004.07881.x

Bruzual, G. & Charlot, S. 2003, MNRAS, 344, 1000. doi:10.1046/j.1365-8711.2003.06897.x

Calzetti, D., Armus, L., Bohlin, R. C., et al. 2000, ApJ, 533, 682. doi:10.1086/308692

Cardelli, J. A., Clayton, G. C., & Mathis, J. S. 1989, ApJ, 345, 245. doi:10.1086/167900

Carniani, S., Marconi, A., Maiolino, R., et al. 2015, A&A, 580, A102. doi:10.1051/0004-6361/201526557

Chabrier, G. 2003, PASP, 115, 763. doi:10.1086/376392

Chapman, S. C., Scott, D., Windhorst, R. A., et al. 2004, ApJ, 606, 85. doi:10.1086/382778

Ciotti, L. & Ostriker, J. P. 2007, ApJ, 665, 1038. doi:10.1086/519833

Ciotti, L., Ostriker, J. P., & Proga, D. 2010, ApJ, 717, 708. doi:10.1088/0004-637X/717/2/708

Cresci, G., Mainieri, V., Brusa, M., et al. 2015, ApJ, 799, 82. doi:10.1088/0004-637X/799/1/82

Dale, D. A., Helou, G., Magdis, G. E., et al. 2014, ApJ, 784, 83. doi:10.1088/0004-637X/784/1/83

Danielson, A. L. R., Swinbank, A. M., Smail, I., et al. 2017, ApJ, 840, 78. doi:10.3847/1538-4357/aa6caf

Davies, R. I., Müller Sánchez, F., Genzel, R., et al. 2007, ApJ, 671, 1388. doi:10.1086/523032

Delhaize, J., Smolčić, V., Delvecchio, I., et al. 2017, A&A, 602, A4. doi:10.1051/0004-6361/201629430

Donnari, M., Pillepich, A., Nelson, D., et al. 2021, MNRAS, 506, 4760. doi:10.1093/mnras/stab1950

- Fabian, A. C. 2012, *ARA&A*, 50, 455.
doi:10.1146/annurev-astro-081811-125521
- Ferrarese, L. & Merritt, D. 2000, *ApJL*, 539, L9.
doi:10.1086/312838
- Fischer, T. C., Machuca, C., Diniz, M. R., et al. 2017, *ApJ*, 834, 30. doi:10.3847/1538-4357/834/1/30
- Fiore, F., Feruglio, C., Shankar, F., et al. 2017, *A&A*, 601, A143. doi:10.1051/0004-6361/201629478
- Foreman-Mackey, D., Hogg, D. W., Lang, D., et al. 2013, *PASP*, 125, 306. doi:10.1086/670067
- Forrest, B., Marsan, Z. C., Annunziatella, M., et al. 2020, *ApJ*, 903, 47. doi:10.3847/1538-4357/abb819
- Fritz, J., Franceschini, A., & Hatziminaoglou, E. 2006, *MNRAS*, 366, 767. doi:10.1111/j.1365-2966.2006.09866.x
- Fluetsch, A., Maiolino, R., Carniani, S., et al. 2019, *MNRAS*, 483, 4586. doi:10.1093/mnras/sty3449
- Fu, H., Yan, L., Myers, A. D., et al. 2012, *ApJ*, 745, 67.
doi:10.1088/0004-637X/745/1/67
- Geach, J. E., Alexander, D. M., Lehmer, B. D., et al. 2009, *ApJ*, 700, 1. doi:10.1088/0004-637X/700/1/1
- Gelderman, R. & Whittle, M. 1994, *ApJS*, 91, 491.
doi:10.1086/191946
- Genzel, R., Förster Schreiber, N. M., Rosario, D., et al. 2014, *ApJ*, 796, 7. doi:10.1088/0004-637X/796/1/7
- Greve, T. R., Bertoldi, F., Smail, I., et al. 2005, *MNRAS*, 359, 1165. doi:10.1111/j.1365-2966.2005.08979.x
- Groves, B. A., Dopita, M. A., & Sutherland, R. S. 2004, *ApJS*, 153, 9. doi:10.1086/421113
- Harrison, C. M., Alexander, D. M., Mullaney, J. R., et al. 2014, *MNRAS*, 441, 3306. doi:10.1093/mnras/stu515
- Harrison, C. M., Alexander, D. M., Mullaney, J. R., et al. 2016, *MNRAS*, 456, 1195. doi:10.1093/mnras/stv2727
- Hayashino, T., Matsuda, Y., Tamura, H., et al. 2004, *AJ*, 128, 2073. doi:10.1086/424935
- Helou, G., Soifer, B. T., & Rowan-Robinson, M. 1985, *ApJL*, 298, L7. doi:10.1086/184556
- Hennawi, J. F., Prochaska, J. X., Kollmeier, J., et al. 2009, *ApJL*, 693, L49. doi:10.1088/0004-637X/693/2/L49
- Hopkins, P. F., Hernquist, L., Cox, T. J., et al. 2006, *ApJS*, 163, 1. doi:10.1086/499298
- Ibar, E., Cirasuolo, M., Ivison, R., et al. 2008, *MNRAS*, 386, 953. doi:10.1111/j.1365-2966.2008.13077.x
- Ichikawa, T., Suzuki, R., Tokoku, C., et al. 2006, *Proc. SPIE*, 6269, 626916. doi:10.1117/12.670078
- Ivison, R. J., Magnelli, B., Ibar, E., et al. 2010, *A&A*, 518, L31. doi:10.1051/0004-6361/201014552
- Jarvis, M. E., Harrison, C. M., Thomson, A. P., et al. 2019, *MNRAS*, 485, 2710. doi:10.1093/mnras/stz556
- Just, D. W., Brandt, W. N., Shemmer, O., et al. 2007, *ApJ*, 665, 1004. doi:10.1086/519990
- Kakkad, D., Mainieri, V., Vietri, G., et al. 2020, *A&A*, 642, A147. doi:10.1051/0004-6361/202038551
- Kauffmann, G., White, S. D. M., Heckman, T. M., et al. 2004, *MNRAS*, 353, 713.
doi:10.1111/j.1365-2966.2004.08117.x
- Kauffmann, G. & Heckman, T. M. 2009, *MNRAS*, 397, 135.
doi:10.1111/j.1365-2966.2009.14959.x
- Kennicutt, R. C. & Evans, N. J. 2012, *ARA&A*, 50, 531.
doi:10.1146/annurev-astro-081811-125610
- Kewley, L. J., Groves, B., Kauffmann, G., et al. 2006, *MNRAS*, 372, 961. doi:10.1111/j.1365-2966.2006.10859.x
- Kodama, T., Arimoto, N., Barger, A. J., et al. 1998, *A&A*, 334, 99
- Kormendy, J. & Ho, L. C. 2013, *ARA&A*, 51, 511.
doi:10.1146/annurev-astro-082708-101811
- Kubo, M., Uchimoto, Y. K., Yamada, T., et al. 2013, *ApJ*, 778, 170. doi:10.1088/0004-637X/778/2/170
- Kubo, M., Yamada, T., Ichikawa, T., et al. 2015, *ApJ*, 799, 38. doi:10.1088/0004-637X/799/1/38
- Kubo, M., Yamada, T., Ichikawa, T., et al. 2016, *MNRAS*, 455, 3333. doi:10.1093/mnras/stv2392
- Kubo, M., Tanaka, M., Yabe, K., et al. 2018, *ApJ*, 867, 1.
doi:10.3847/1538-4357/aae3e8
- Kubo, M., Umehata, H., Matsuda, Y., et al. 2021, *ApJ*, 919, 6. doi:10.3847/1538-4357/ac0cf8
- Law, D. R., Steidel, C. C., Chen, Y., et al. 2018, *ApJ*, 866, 119. doi:10.3847/1538-4357/aae156
- Lehmer, B. D., Alexander, D. M., Geach, J. E., et al. 2009a, *ApJ*, 691, 687. doi:10.1088/0004-637X/691/1/687
- Lehmer, B. D., Alexander, D. M., Chapman, S. C., et al. 2009b, *MNRAS*, 400, 299.
doi:10.1111/j.1365-2966.2009.15449.x
- Lemaux, B. C., Lubin, L. M., Shapley, A., et al. 2010, *ApJ*, 716, 970. doi:10.1088/0004-637X/716/2/970
- Leung, G. C. K., Coil, A. L., Azadi, M., et al. 2017, *ApJ*, 849, 48. doi:10.3847/1538-4357/aa9024
- Leung, G. C. K., Coil, A. L., Aird, J., et al. 2019, *ApJ*, 886, 11. doi:10.3847/1538-4357/ab4a7c
- Liu, G., Zakamska, N. L., Greene, J. E., et al. 2013, *MNRAS*, 436, 2576. doi:10.1093/mnras/stt1755
- Liu, T., Tozzi, P., Wang, J.-X., et al. 2017, *ApJS*, 232, 8.
doi:10.3847/1538-4365/aa7847
- Madau, P. & Dickinson, M. 2014, *ARA&A*, 52, 415.
doi:10.1146/annurev-astro-081811-125615
- Magorrian, J., Tremaine, S., Richstone, D., et al. 1998, *AJ*, 115, 2285. doi:10.1086/300353
- Marchesi, S., Civano, F., Elvis, M., et al. 2016, *ApJ*, 817, 34. doi:10.3847/0004-637X/817/1/34
- Marconi, A., Risaliti, G., Gilli, R., et al. 2004, *MNRAS*, 351, 169. doi:10.1111/j.1365-2966.2004.07765.x

- Matsuda, Y., Yamada, T., Hayashino, T., et al. 2004, *AJ*, 128, 569. doi:10.1086/422020
- McConachie, I., Wilson, G., Forrest, B., et al. 2021, arXiv:2109.07696
- McLean, I. S., Steidel, C. C., Epps, H. W., et al. 2012, *Proc. SPIE*, 8446, 84460J. doi:10.1117/12.924794
- Mignoli, M., Feltre, A., Bongiorno, A., et al. 2019, *A&A*, 626, A9. doi:10.1051/0004-6361/201935062
- Mizukoshi, S., Kohno, K., Egusa, F., et al. 2021, *ApJ*, 917, 94. doi:10.3847/1538-4357/ac01cc
- Monson, E. B., Lehmer, B. D., Doore, K., et al. 2021, *ApJ*, 919, 51. doi:10.3847/1538-4357/ac0f84
- Mukherjee, D., Bicknell, G. V., Sutherland, R., et al. 2016, *MNRAS*, 461, 967. doi:10.1093/mnras/stw1368
- Mullaney, J. R., Alexander, D. M., Aird, J., et al. 2015, *MNRAS*, 453, L83. doi:10.1093/mnras/slv110
- Murphy, E. J. 2009, *ApJ*, 706, 482. doi:10.1088/0004-637X/706/1/482
- Naab, T. & Burkert, A. 2003, *ApJ*, 597, 893. doi:10.1086/378581
- Nesvadba, N. P. H., Lehnert, M. D., Eisenhauer, F., et al. 2006, *ApJ*, 650, 693. doi:10.1086/507266
- Norman, C. & Scoville, N. 1988, *ApJ*, 332, 124. doi:10.1086/166637
- Norman, C., Hasinger, G., Giacconi, R., et al. 2002, *ApJ*, 571, 218. doi:10.1086/339855
- O’Dea, C. P. 1998, *PASP*, 110, 493. doi:10.1086/316162
- Osterbrock, D. E. & Ferland, G. J. 2006, *Astrophysics of gaseous nebulae and active galactic nuclei*, 2nd. ed. by D.E. Osterbrock and G.J. Ferland. Sausalito, CA: University Science Books, 2006
- Panessa, F., Baldi, R. D., Laor, A., et al. 2019, *Nature Astronomy*, 3, 387. doi:10.1038/s41550-019-0765-4
- Revalski, M., Crenshaw, D. M., Kraemer, S. B., et al. 2018, *ApJ*, 856, 46. doi:10.3847/1538-4357/aab107
- Rosario, D. J., Santini, P., Lutz, D., et al. 2012, *A&A*, 545, A45. doi:10.1051/0004-6361/201219258
- Rupke, D. S. N. & Veilleux, S. 2011, *ApJL*, 729, L27. doi:10.1088/2041-8205/729/2/L27
- Rupke, D. S. N. & Veilleux, S. 2013, *ApJ*, 768, 75. doi:10.1088/0004-637X/768/1/75
- Santini, P., Rosario, D. J., Shao, L., et al. 2012, *A&A*, 540, A109. doi:10.1051/0004-6361/201118266
- Santini, P., Merlin, E., Fontana, A., et al. 2019, *MNRAS*, 486, 560. doi:10.1093/mnras/stz801
- Sanders, R. L., Shapley, A. E., Kriek, M., et al. 2016, *ApJ*, 816, 23. doi:10.3847/0004-637X/816/1/23
- Saracco, P., Marchesini, D., La Barbera, F., et al. 2020, *ApJ*, 905, 40. doi:10.3847/1538-4357/abc7c4
- Schawinski, K., Thomas, D., Sarzi, M., et al. 2007, *MNRAS*, 382, 1415. doi:10.1111/j.1365-2966.2007.12487.x
- Schreiber, C., Glazebrook, K., Nanayakkara, T., et al. 2018, *A&A*, 618, A85. doi:10.1051/0004-6361/201833070
- Shi, K., Toshikawa, J., Lee, K.-S., et al. 2021, *ApJ*, 911, 46. doi:10.3847/1538-4357/abe62e
- Shibuya, T., Ouchi, M., & Harikane, Y. 2015, *ApJS*, 219, 15. doi:10.1088/0067-0049/219/2/15
- Shimizu, T. T., Mushotzky, R. F., Meléndez, M., et al. 2015, *MNRAS*, 452, 1841. doi:10.1093/mnras/stv1407
- Smolčić, V., Novak, M., Bondi, M., et al. 2017, *A&A*, 602, A1. doi:10.1051/0004-6361/201628704
- Sparre, M. & Springel, V. 2016, *MNRAS*, 462, 2418. doi:10.1093/mnras/stw1793
- Steidel, C. C., Adelberger, K. L., Dickinson, M., et al. 1998, *ApJ*, 492, 428. doi:10.1086/305073
- Strom, A. L., Steidel, C. C., Rudie, G. C., et al. 2018, *ApJ*, 868, 117. doi:10.3847/1538-4357/aae1a5
- Sutherland, R. S. & Dopita, M. A. 1993, *ApJS*, 88, 253. doi:10.1086/191823
- Suzuki, R., Tokoku, C., Ichikawa, T., et al. 2008, *PASJ*, 60, 1347. doi:10.1093/pasj/60.6.1347
- Tacconi, L. J., Neri, R., Chapman, S. C., et al. 2006, *ApJ*, 640, 228. doi:10.1086/499933
- Tamura, Y., Iono, D., Wilner, D. J., et al. 2010, *ApJ*, 724, 1270. doi:10.1088/0004-637X/724/2/1270
- Tanaka, M., Valentino, F., Toft, S., et al. 2019, *ApJL*, 885, L34. doi:10.3847/2041-8213/ab4ff3
- Toba, Y., Yamashita, T., Nagao, T., et al. 2019, *ApJS*, 243, 15. doi:10.3847/1538-4365/ab238d
- Toft, S., Smolčić, V., Magnelli, B., et al. 2014, *ApJ*, 782, 68. doi:10.1088/0004-637X/782/2/68
- Tremonti, C. A., Heckman, T. M., Kauffmann, G., et al. 2004, *ApJ*, 613, 898. doi:10.1086/423264
- Ueda, Y., Hashimoto, Y., Ichikawa, K., et al. 2015, *ApJ*, 815, 1. doi:10.1088/0004-637X/815/1/1
- Umehata, H., Tamura, Y., Kohno, K., et al. 2015, *ApJL*, 815, L8. doi:10.1088/2041-8205/815/1/L8
- Umehata, H., Tamura, Y., Kohno, K., et al. 2017, *ApJ*, 835, 98. doi:10.3847/1538-4357/835/1/98
- Umehata, H., Hatsukade, B., Smail, I., et al. 2018, *PASJ*, 70, 65. doi:10.1093/pasj/psy065
- Umehata, H., Fumagalli, M., Smail, I., et al. 2019, *Science*, 366, 97. doi:10.1126/science.aaw5949
- Valentino, F., Tanaka, M., Davidzon, I., et al. 2020, *ApJ*, 889, 93. doi:10.3847/1538-4357/ab64dc
- Villar-Martín, M., Humphrey, A., Delgado, R. G., et al. 2011, *MNRAS*, 418, 2032. doi:10.1111/j.1365-2966.2011.19622.x

- Webb, T. M. A., Yamada, T., Huang, J.-S., et al. 2009, ApJ, 692, 1561. doi:10.1088/0004-637X/692/2/1561
- Weinberger, R., Springel, V., Hernquist, L., et al. 2017, MNRAS, 465, 3291. doi:10.1093/mnras/stw2944
- Whitaker, K. E., van Dokkum, P. G., Brammer, G., et al. 2013, ApJL, 770, L39. doi:10.1088/2041-8205/770/2/L39
- Wild, V., Heckman, T., & Charlot, S. 2010, MNRAS, 405, 933. doi:10.1111/j.1365-2966.2010.16536.x
- Xu, C., Livio, M., & Baum, S. 1999, AJ, 118, 1169. doi:10.1086/301007
- Yan, R., Newman, J. A., Faber, S. M., et al. 2006, ApJ, 648, 281. doi:10.1086/505629
- Yang, G., Brandt, W. N., Luo, B., et al. 2016, ApJ, 831, 145. doi:10.3847/0004-637X/831/2/145
- Yang, G., Boquien, M., Buat, V., et al. 2020, MNRAS, 491, 740. doi:10.1093/mnras/stz3001
- Zakamska, N. L. & Greene, J. E. 2014, MNRAS, 442, 784. doi:10.1093/mnras/stu842